Studies of the periodic faceting of epitaxial molybdenum oxide grown on Mo(110)

K. Radican,* N. Berdunov,† and I. V. Shvets
School of Physics, CRANN, Trinity College, Dublin 2, Ireland
(Received 4 December 2007; published 13 February 2008)

We show that an oxide film can undergo a periodic self-faceting regime during growth. The oxide growth starts as a bulklike MoO_2 surface oxide trilayer that wets the substrate in an orientation thermodynamically forbidden in the bulk. As this film continues to grow, it develops into a periodically faceted surface with nanowirelike structures composed of MoO_2 (0 2 1) and (0 2 −1) faces. Through the use of density functional theory, it is found that this faceted surface has a lower surface free energy than the initial growth orientation. Finally, using the theory of faceted surfaces, we demonstrate that the periodicity of the facets is likely an equilibrium state that is related to the elastic properties of the film.

DOI: 10.1103/PhysRevB.77.085417 PACS number(s): 68.47.Gh, 68.65.La, 81.16.−c

I. INTRODUCTION

In recent years, there has been extraordinary effort placed into developing new methods and techniques to build nanoscale structures and devices.[1–5] The formation of quantum dots and wires of epitaxially grown thin solid films has been attracting attention as a very promising area of nanotechnology that could lead to a new generation of electronic devices. We present here a simple and robust technique of forming uniform nanowire arrays composed of molybdenum oxide.

Recently, Golovin *et al.* proposed a mechanism for the formation of quantum dots on the surface of thin solid films.[6] This method is a bottom-up approach in which the film goes through two stages of growth. In the initial growth stage, the film is coupled to the substrate via a strong wetting interaction. Furthermore, the substrate dictates the film to grow in a crystallographic orientation that, due to a large surface energy anisotropy, would be thermodynamically forbidden in the bulk and prone to faceting. However, due to the adhesion energy associated with the wetting interaction, the faceting is suppressed. Stage two occurs upon further film growth with which the short ranged stabilizing effects of the wetting interaction can no longer stabilize the film surface, resulting in periodic faceting of the film surface. Furthermore, it is important that this type of growth should not be confused with the Asaro-Tiller-Grinfel'd (ATG) instability commonly used to form nanodots.[7,8] With ATG, the onset of island growth is triggered by a strain relaxation of the film due to a misfit with the substrate, whereas, in this case, we have a transition to a periodically faceted surface to accommodate the divergent surface energy of the Tasker type III metal-oxygen-metal (O-*M*-O) oxide surface.[9]

In a previous paper, we showed that in the first stage of oxide growth on the Mo(110) surface is a highly strained closed MoO_2 (010) layer.[10] However, in the bulk, this (010) oxide surface can be classified as a polar, Tasker type III surface, which needs a surface modification to be energetically favorable.[9] In the case of the MoO_2 (010) surface oxide, as with any metal-to-polar oxide interface, the oxide film surface is close enough to the interface such that a charge redistribution at the interface can sufficiently modify the surface charge density and stabilize the film.[11–15] However, a key difference of this system is that the O-*M*-O oxide layer is not a transient surface oxide phase like with the other studies, but it is that of the bulk oxide, MoO_2 (0 1 0). Therefore, with further oxidation, the oxide phase would continue to grow. In the following, we will use the MoO_2 (0 1 0) surface oxide as our starting point and show that with continued oxidation, MoO_2 grown on Mo(110) meets the criteria for this mechanism. As a result the oxide film develops into regular arrays of MoO_2 nanowires. As MoO_2 is a metallic oxide that makes these conductive wires applicable for fundamental research as well as for industrial technologies. Furthermore, we have preliminary results of using this method to produce these structures as nanowire arrays positioned on an insulating substrate (not shown).

II. EXPERIMENTAL PROCEDURE

In this experiment, we used the same sample and cleaning procedure as outlined previously.[10] Once a clean surface was obtained, the samples were annealed by using the following procedure. First, the UHV chamber was back-filled with oxygen to a pressure of 1×10^{-6} Torr. The sample temperature was then ramped from room temperature to 1200 ± 50 °C (beyond the decomposition temperature of molybdenum oxides), at a rate of approximately 300 °C/min, and then down to 900 ± 50 °C. The sample was held at 900 ± 50 °C for the desired annealing time and then cooled in an oxygen environment at a ramp rate of approximately 100 °C/min. After the samples were cooled to room temperature, the surfaces were characterized using low-energy electron diffraction (LEED), Auger electron spectroscopy (AES), and scanning tunneling microscopy (STM). All STM images were recorded at room temperature in the constant current mode using currents of approximately 0.05–0.1 nA and bias voltages of 0.1–0.05 V, with electrochemically etched W tips. The STM used in these studies was calibrated for atomic scale measurements. However, due to the relatively large size of these features, along with a lack of a nanometer scale calibration standard, we have introduced a larger degree of error in these measurements. The STM images were analyzed with the WSXM software package.[16]

III. RESULTS AND DISCUSSION

In order to characterize the oxidation of Mo(110) under these conditions, the sample was annealed with a series of

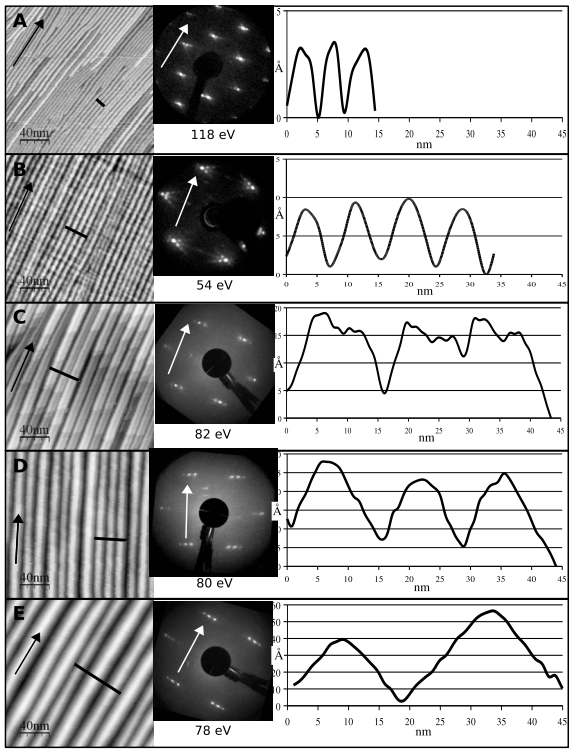

FIG. 1. LEED, STM, and line profiles of the Mo(110) surface after annealing, showing the development of MoO_2 nanowires over time. The images marked A, B, C, D, and E correspond to the surface after annealing for 5, 10, 15, 30, and 60 min, respectively. The arrows in the LEED and STM images show the Mo(001) direction. The width and height of the structures have the following dimensions, respectively: (A) 5.20×0.33 nm^2, (B) 8.46×1.00 nm^2, (C) 14.42×1.4 nm^2, (D) 15.32×2.5 nm^2, and (E) 27.50×5 nm^2. The direction of the line profile is shown in the STM image by a solid line.

anneals from 5 to 90 min. After each anneal, the sample was analyzed with LEED and STM, and then flashed clean before starting another anneal. The series of LEED and STM images in Fig. 1 show the evolution of molybdenum oxide over a range of annealing times from 5 min [Fig. 1(a)] up to 1 h [Fig. 1(e)]. The resulting oxide has the form of nanowires. These wires grow in the Mo(110) [001] direction and have dimensions ranging from 5 nm wide by 0.5 nm tall up to a maximum size of 30 nm wide by 6 nm tall. These are shown by the line profiles in Fig. 1. Remarkably, the direction of the wirelike structures is different from the direction of the stripes observed at an earlier stage of the oxidation process.[10] This indicates that the initial surface strain caused by coincidence structure of the surface oxide is no longer a source of surface arrangement. What is most interesting is that the dimensions of these wires are solely dependent on the annealing time, allowing the size of the wires to be easily manipulated. However, with further annealing beyond 1 h, wires larger than 30 nm wide could not be achieved.

A. Scanning tunneling microscopy analysis

Attempts were made to view the atomic structure of these wires with STM; however, such resolution could not be achieved. There is, however, further information about the structure of these wires in the STM measurements. Figure 2 shows a high-resolution STM image of a side of one of the large nanowires. In this image, terraces can be seen. According to the line profile in this figure, one can see that the largest nanowires are comprised of terraces that have a width of 0.95 ± 0.09 nm and a step height of 0.53 ± 0.05 nm (Fig. 2). These dimensions give a slope of $\sim 30°$ to the substrate surface normal, resulting in a periodically faceted "hill and valley" MoO_2 surface.

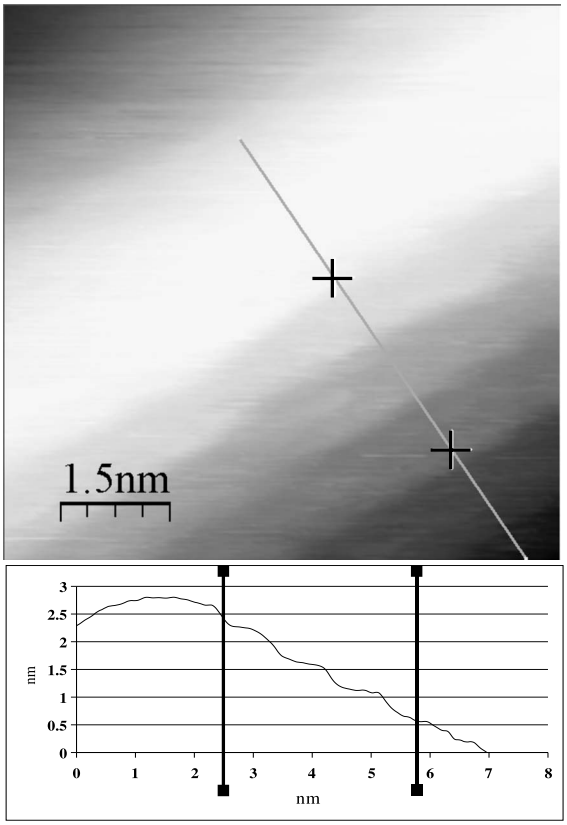

FIG. 2. STM image of the profile of a large oxide wire. The line profile shows terraces of 0.95 ± 0.09 nm wide 0.53 ± 0.05 nm tall.

B. Auger data

The Auger spectra of the largest wires indicate that the oxide has the stoichiometry of MoO_2 (Fig. 3). The ratio of the Mo peak to the oxygen peak at 510 eV is 1:2. The relative atomic concentration of Mo and O at the surface are listed in Table I.

C. Low-energy electron diffraction analysis

The LEED pattern in Fig. 1(a) is that of Mo(110) with satellite spots along Mo [1 −1 −3] and [1 −1 3] directions, similar but more diffuse to that seen previously.[10] In Fig. 1(b), the satellite spots seen in Fig. 1(a) have become even more diffuse, and a different spot has developed along Mo. [1 −1 0] In Figs. 1(c)–1(e), the pattern, though still quasihexagonal, no longer has spots representative of Mo(110).

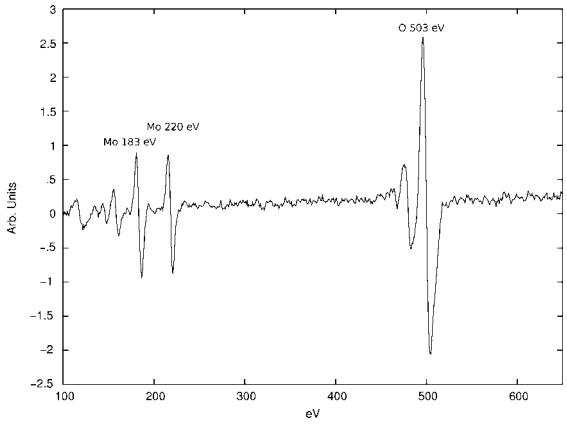

FIG. 3. Auger spectra of the MoO_2 oxide surface.

Figure 4 shows a close-up of the LEED pattern taken of the surface structure shown in Fig. 1(c). This pattern gives a quasihexagonal structure with a lattice constant of 2.7 ± 0.3 Å and an angle of $61° \pm 1°$. These dimensions make this pattern an unsuitable match for Mo(110), which has dimensions 2.7 Å but an angle of 70°, and, therefore, it must be that of the molybdenum oxide. However, with a unit cell of $a=5.611$ Å, $c=5.628$ Å, and $\beta=120.95°$, the LEED pattern is not what one would expect for the $MoO_2(010)$ unit cell (Fig. 1).[17] The fact that there is a glide plane along the MoO_2 c axis can explain missing odd order spots along that direction, but cannot explain the missing spots along the a axis. Transmission high-energy electron diffraction images along the $Mo_2(010)$ direction show weak odd order spots with bright even order spots.[18] It is possible that the odd order spots are too weak to be detected with our LEED setup. Another explanation may be that since the pattern is close in orientation and dimension to that of the $MoO_2(010)$ oxygen layer, the pattern is the result of the oxygen unit cell at the surface or, perhaps, a surface reconstruction. In the following discussion, we will assume no missing spots.

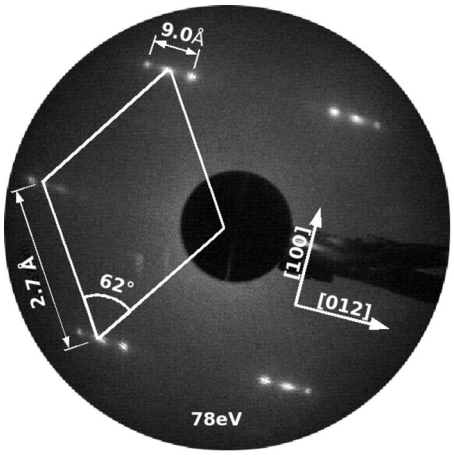

FIG. 4. LEED pattern taken at 78 eV of the surface structure shown in Fig. 1(c). This pattern gives a quasihexagonal structure with a lattice constant of 2.7 ± 0.3 Å and an angle of $62° \pm 1°$.

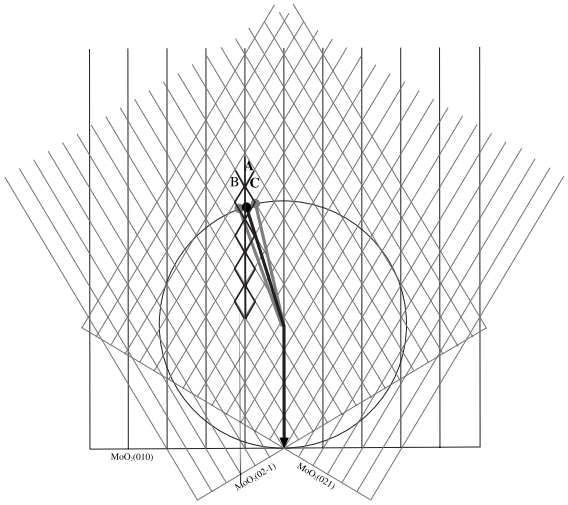

FIG. 5. Ewald sphere diagram for the MoO_2 hill and valley surface. The black vertical lines represent the lattice rods from the $MoO_2(010)$ surface, and the gray tilted lines represent the lattice rods from the terrace edges making up the $MoO_2(021)$ and $(02-1)$ surfaces.

D. Low-energy electron diffraction spot splitting

Another interesting feature of the LEED patterns from Figs. 1(c)–1(e) is the presence of periodic splitting of the LEED spots over a range of beam energies. The splitting is well known and is an indication of regular step arrays on the surface.[19,20] This is explained by the superposition of the diffraction from atoms at the terraces and from atoms at the step edges. With one-dimensional step arrays, by changing energy, there is a periodic appearance of single and of split integer-order LEED spots. However, in this case, doublets of spots open and close to single spots. This is an indication of both ascending and descending staircases on the surface, as expected from the STM data. To further describe this, a diagram of the Ewald sphere for this system is drawn in Fig. 5. In this figure, the rods coresponding to the (0,1) spots are highlighted with bold black lines labeled A, B, and C.

To illustrate the splitting, the graph of Fig. 6 shows a series of line profiles along the MoO_2 [012] direction of the (0,1) and (1,0) LEED spots. The line profiles are taken over a range of beam energies from 58 to 173 eV, and show that there are three distinct phases of spots over this energy range. Starting at 58 eV, there is one (0,1) and one (1,0) LEED spot. With increasing energy, the spots split in two. As the energy increases beyond 68 eV, the spots continue to split apart. At 78 eV, the primary (0,1) and (1,0) spots become visible again. Furthermore, at this energy, the maxi-

TABLE I. Relative atomic concentrations of Mo and O from AES of a MoO_2 film.

Species	Concentration
Mo	35%
O	65%

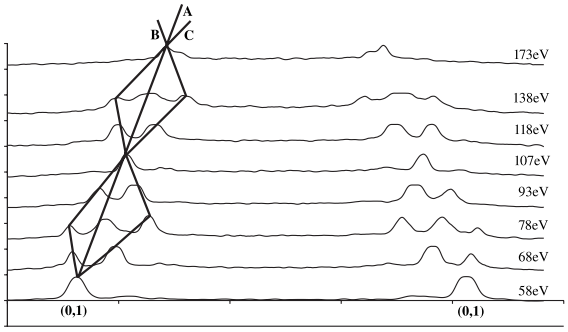

FIG. 6. Graph of the LEED spot profile taken along the MoO_2 [102] direction at various beam energies. The bold line marked A shows the position of the (0,1) spot, and the bold lines B and C show the positions of the spot splitting satellites.

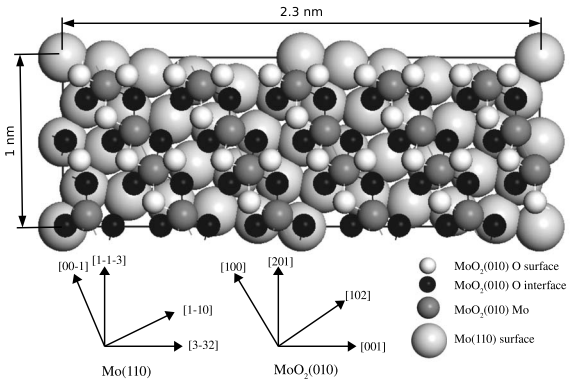

FIG. 7. Diagram showing the epitaxy of the $MoO_2(010)$ layer on Mo(110).

mum separation between two symmetric multiplet spots occurs as a result of spots from diffraction at ascending and descending steps coinciding. Therefore, the separation of the spots at this point is related to the average terrace width, allowing this value to be directly measured from LEED. We measured this value to be 9.0 ± 0.9 Å. As the energy continues to increase, the primary spots disappear again and the two spots begin to coalesce until at an energy of 107 eV, only one primary spot is visible. To help visualize this for the reader, the bold black lines labeled A, B, and C trace the path of the (0,1) LEED spots with changing energy in Fig. 6, and is representative of the bold lines A, B, and C of the Ewald sphere in Fig. 5 mentioned above.

The energy of the singular LEED spot which appears and disappears is related to the in-phase and out-of-phase scattering of electrons of adjacent terraces, respectively. Therefore, the "characteristic" beam energies at which they occur is a function of the step height and lattice parameter of the surface in the direction of the splitting. This was originally described by Henzler, from which we obtain the equation[19]

$$E(s) = \frac{\hbar^2}{2m_0}\left(\frac{\pi}{r}\right)^2\left[\left(s + \frac{g}{a}\right)^2 + \frac{r^2}{a^2}\right], \tag{1}$$

where s is the order of the splitting; $\hbar$ and m_0 are Planck's constant and the electron mass, respectively; r and a are the step height and lattice constant in the direction of splitting, respectively; and g is a fitting parameter to account for a horizontal offset at the lower step edge.

Using the measured value of the lattice constant from the LEED images, along with the voltages at which the primary spots occur, we can calculate the average step height with the following equation:

$$E(s+1) - E(s) = \frac{\hbar^2}{m_0}\left(\frac{\pi}{r}\right)^2\left[s + \left(\frac{g}{a} + \frac{1}{2}\right)\right]. \tag{2}$$

From this, we have an average step height of 4.6 Å. This value r is in agreement with the STM measurements, and close to the 4.86 Å value of the MoO_2 b axis.

From these experimental results, in addition to previous information about the oxidation of Mo(110), we can develop a structural model for the formation of these nanowires. This model will be described in the following section.

E. Nanowire model

As the basis for a model of the molybdenum oxide nanowires, we will start with the surface oxide model described previously.[10] For reference, Fig. 7 shows the unit cell of $MoO_2(010)$ oxide that forms a coincident lattice structure with the Mo(110) surface. The orientation of the MoO_2 overlayer is such that $MoO_2[201] \| Mo[1-1-3]$ and $MoO_2[001] \| Mo[3-3\ 2]$, as shown in Fig. 7. With this orientation, it can be seen that there are Mo-Mo dimer rows that form chains aligned with the MoO_2 a axis and close to the Mo(110) $[00-1]$ direction, which is the same direction as the nanowires. Therefore, it is likely that the growth of the nanowires is related to these chains and that the chains are the building blocks that form the nanowires.

To describe the self-assembly of the oxide nanowires, a unit cell to be used as a "building block" needs to be constructed. For the basis of this unit cell, we used the orientation of the MoO_2 overlayer described above. Therefore, the cell of MoO_2 has a base in the (010) plane, with one side being the MoO_2 a axis, which defines the direction of the nanowires. The second side has one unit length in the [102] direction, perpendicular to the wires, and width of 9.66 Å, in agreement with the terrace width measured in LEED and STM. Furthermore, if we make this cell one unit tall along the b axis, we have a MoO_2 "block" with a height of 4.86 Å, within the error of the terrace height measured by LEED and STM (Fig. 8) and of the height of the smallest wires measured in Fig. 1.

This building block can now be used to illustrate the assembly of the MoO_2 nanowires. Starting with the smallest wires, which we measured to be ~57 Å wide and ~5 Å tall. The wire height of ~5 Å can easily be associated with the height of one MoO_2 unit cell. However, to get the minimum width, we also need to know the dimensions of the Mo(110) substrate. Comparing the dimensions of the Mo $[1-1\ 0]$ and the MoO_2 [102] unit length, which in the diagram in Fig. 7 are ~5° apart, we see that there is a 13:6 relationship between them, giving a smallest common integer length of 58 Å. Therefore, while the initial surface oxide layer grows

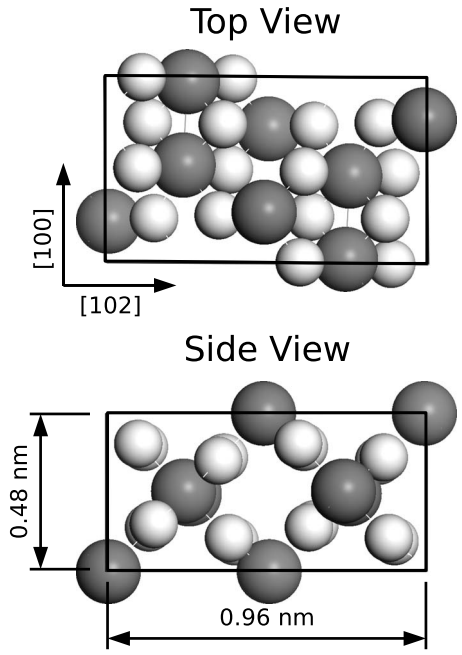

FIG. 8. Diagram of the MoO_2 building block.

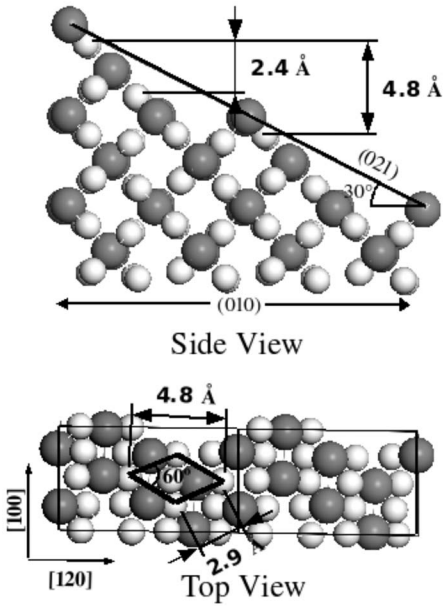

FIG. 10. An atomic model of the side and top views, respectively, of the oxide facet structure with the planes identified.

as highly a strained wetting layer, it is likely that with the onset of three-dimensional growth, this changes to a less strained MoO_2 oxide layer which runs along the MoO_2 [100] direction, and is six units wide in the [102] direction. This results in regular arrays of oxide nanowires in the MoO_2 [100] direction.

As the oxide continues to grow, the oxide building blocks continue to assemble and, according to the annealing time, form various sizes of wires, as represented graphically in Fig. 9.

With regard to the largest wires, first, we can determine the orientation of the two surface facets that make up the sides of the wires. From the above model, and in agreement with the slope of faces as measured by STM, we determined the surfaces to be $MoO_2(021)$ and $(02-1)$ (Fig. 10). The (0 2 1) surface (Fig. 11) has previously been identified as a stable low-energy surface for rutile and distorted rutile oxides.[21–23] The stability of the distorted rutile (0 1 2), (0 2 1) and rutile (2 1 0) surface stems from it being made of charge balanced M_2O_4 layers (Tasker type II), thus eliminating the need for a charge redistribution to lower the surface energy of the initial MoO_2 (0 1 0) type III surface.

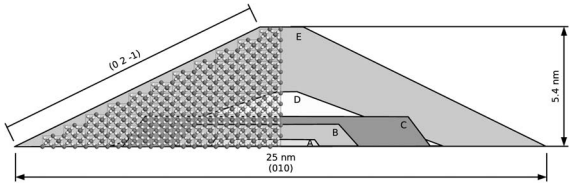

FIG. 9. Cross section of the various MoO_2 wire sizes measured by us with STM, corresponding to various anneal times. Wires A, B, C, D, and E are the same as in Fig. 1. The assembly of MoO_2 building blocks is shown for comparison.

F. Surface energy calculations

In order to quantify this, we employed density functional theory (DFT) total energy calculations to determine the surface energy for the MoO_2 (0 1 0) and (0 2 1) surfaces. Furthermore, for comparison, we also calculated the surface energy of the MoO_2 (0 1 1) surface, which is commonly considered the lowest energy rutile surface.[21] For the calculations, we used the conventional approach in which the surface energy γ is determined by

$$\gamma = (E_{slab} - NE_{bulk})/2A, \tag{3}$$

where E_{slab} is the total energy of a slab of MoO_2 crystal cleaved to the desired orientation, N is the number of layers in the slab, A is the area of the surface, and E_{bulk} is the total energy of a bulk layer. For the calculations, we employed

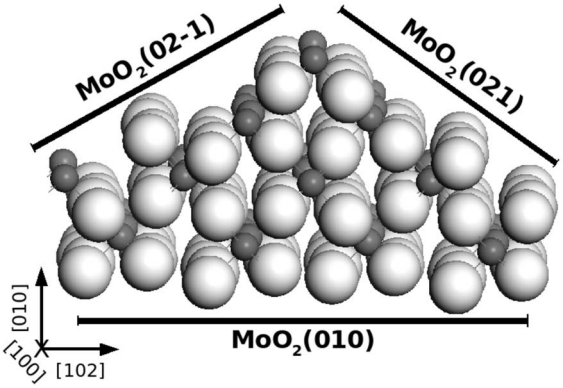

FIG. 11. A diagram of the oxide facet structure with the planes identified. The white spheres are oxygen atoms and the gray spheres are molybdenum atoms. It is a slice taken in the (2 0 −1) plane looking along the a axis (along the faceted rows).

TABLE II. DFT Calculated surface energy.

{hkl}	γ_{hkl} (J/m^2)	$\frac{\gamma_{hkl}}{\cos(\phi)}$
{010}	3.38	3.38
{021}	1.91	2.11
{011}	1.28	1.81

VASP with projector augmented wave local density approximation (LDA) pseudopotentials with Ceperley-Alder (CA) exchange functional.[24–27] For all geometries, five unit layer slabs were used, each containing 60 atoms, except for the (010), which contained 59 in order to provide oxygen terminations at each surface. We used Γ centered $(8\times8\times1)$ k-point grids for the two low index surfaces and a $(4\times8\times1)$ k-point grid for the (021) surface. The middle layer was constrained, allowing the others to relax by minimizing the Hellman-Feynman forces to less that 0.01 eV/Å. The calculated surface energies resulting from these calculations are listed in Table II.

G. Theory of periodic faceting

We have now shown with DFT that the faceted MoO_2 (0 2 1) and (0 2 −1) surfaces would have a lower surface energy than the original (0 1 0) surface. However, to fully describe the surface energy of a periodically faceted hill and valley surface, we must employ the elastic theory of a periodically faceted surface, developed by Andreev and Marchenko.[28,29] This theory has been used to describe the periodic faceting of many surfaces including vicinal metals, Si (113) and Al_2O_3 (10−10).[30–32]

The basis of the theory is that the surface free energy of this type of surface is a competition between the surface energy $F(D)$ of the faces of length (D) and the energy of the convex and concave edges where two faces meet. This is illustrated in Fig. 12 and is described by the equation

$$F(D) = \frac{\gamma(\phi)}{\cos(\phi)} + \frac{\eta(\phi)}{D} - \frac{C(\phi)\tau^2}{YD}\left|\frac{D}{a}\right|, \tag{4}$$

where $\gamma(\phi)$ is the surface free energy, η is the average energy of the concave and convex edges per unit length, C is a geometric factor accounting for the symmetry of the intrinsic surface stress tensor τ, Y is Young's modulus, and a is the lattice parameter. From this equation, there exists an optimal

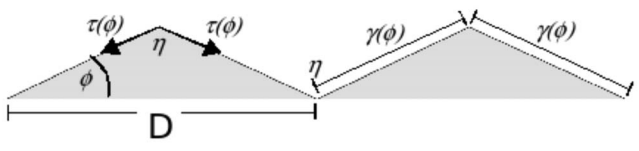

FIG. 12. Illustration of a periodically faceted surface where $\gamma(\phi)$ is the surface free energy, η is the average energy of the concave and convex edges per unit length, the intrinsic surface stress tensor τ, Y is Young's modulus, and periodicity D_{min}, which defines the lowest energy surface.

periodicity D_{min} which defines the lowest energy surface.

$$D_{min} = a\exp\left(\frac{\eta(\phi)Y}{C(\phi)\tau^2} + 1\right). \tag{5}$$

As there is little information available on the elastic properties of MoO_2, the determination of D_{min} for this system is not readily possible. However, this too can be calculated with DFT. In this case, we employed CASTEP due to its integrated algorithm for this purpose. In this case, we used LDA ultrasoft pseudopotentials with the Ceperley-Alder-Perdew-Zunger (CA-PZ) exchange correlation functional[28,33,34] and a $(8\times8\times8)$ k-point grid centered at the γ point. We first obtained the equilibrium primitive cell of MoO_2 by relaxing the ions and cell parameter. We then deformed the cell by applying homogeneous strains of ±0.005 and 0.010, and calculated the resulting stresses. This was done with ion positions fixed so in the strained lattice only the electrons were relaxed. From these results, we were able to determine the 20 elastic constants for the monoclinic MoO_2 crystal, from which it is easy to determine Young's modulus along the three crystallographic axes.[35] Y_a=339.60 GPa, Y_b=184.34 GPa, and Y_c=221.80 GPa. It has been shown that this method can reliably determine the elastic constants of oxides.[36]

By making some reasonable assumptions for the unknown values used in Eq. (5), along with the calculated values from above and the measured periodicity from STM as D_{min}, we arrive at an acceptable value for τ. We used η=20 meV/Å, Y=200 GPa and C=1, giving τ=1.66 J/m^2. Considering that the surface stress τ is the strain derivative per unit area of the surface energy, it follows that the approximation τ=1.66 J/m^2 is a reasonable value for a surface with an energy of 1.91 J/m^2.[37] Therefore, it is reasonable that the 30 nm periodicity of the facets is D_{min}, and the system is at equilibrium according to Marchenko's theory.

Now, if we take another look at Fig. 11, one can see the unidirectional anisotropy of this faceted surface, i.e., there are rows of oxygen atoms and Mo-Mo dimers that run along the MoO_2 [1 0 0] direction (into the page), whereas Mo and O atoms alternate along the [1−1 2] and [1 1 2] directions (along the facets). This anisotropy is also reflected in the elastic properties of the crystal and, therefore, it is related to the direction of the faceting of the surface. From the previously calculated values for Young's modulus, we can see that in the direction along the facets, between the b and c axes, the value is ~200 GPA. However, along the wires in the direction of the a axis, the value is Y=340 GPa. Since $D_{min}\approx e^{kY}$, it is easy to understand why the crystal facets in a direction perpendicular to the MoO_2 a axis.

The results of these calculations are reassuring. They show that by having a faceted surface with (0 2 1) and (0 2 −1) facets, the film will have a lower surface energy than with the original (0 1 0) orientation. Therefore, we have a case where the substrate initially causes a film to grow in an orientation that is normally forbidden, but an electron redistribution at the interface causes the film to wet the substrate's surface. However, the stability effect of the interface is localized, and as the film continues to grow, the MoO_2 (0

1 0) surface becomes unstable and this, coupled to a surface energy anisotropy, leads to the spontaneous formation of a periodically faceted MoO_2 surface with lower energy (0 2 1) and (0 2 −1) faces. Furthermore, a faceting period of ~30 nm is likely an equilibrium state for this surface.

IV. CONCLUSIONS

We have shown that an oxide film can undergo a periodic self-faceting regime during growth. Initially, the oxide grows as a bulklike MoO_2 surface oxide trilayer that wets the substrate in an orientation thermodynamically forbidden in the bulk. After continuing to anneal this surface at 900 °C and $1 \times 10-6$ Torr oxygen, MoO_2 nanowires begin to form.

Through the use of LEED, AES, STM, and DFT, we have fully characterized the growth of these wires. The general idea is that the initial MoO_2 (010) layer is close enough to the interface such that a charge redistribution at the interface can sufficiently modify the surface charge density and stabilize the film. This effect is such that the film fully wets the substrate. As the oxide grows thicker, however, this (010) oxide surface orientation is classified as a polar, Tasker type III surface and requires a surface modification to be energetically favorable.

As this film continues to grow, it develops various sizes of nanowires and eventually develops into a periodically faceted surface made of MoO_2 (0 2 1) and (0 2 −1) faces. Employing *ab initio* calculations, we show that this faceted surface has a lower surface free energy than the initial growth orientation. Furthermore, with the theory of periodically faceted surfaces, we showed that it is likely that the periodicity of the facets, D_{min}, corresponds to a thermodynamically stable surface.

ACKNOWLEDGMENTS

Funding for this project was provided by Science Foundation Ireland Principal Investigator Grant No. 06/IN.1/I91. The authors wish to thank TCHPC for the use of their computing facilities. These facilities were provided by the IITAC research project, funded by the HEA PRTLI Cycle 3 program, the HEA, and the National Development Plan.

*radicak@tcd.ie

†Present address: School of Physics and Astronomy, University Park, Nottingham NG7 2RD, UK.

[1] H. Ibach, Surf. Sci. Rep. **29**, 195 (1997).

[2] A. Mugarza, A. Mascaraque, V. Repain, S. Rousset, K. N. Altmann, F. J. Himpsel, Y. M. Koroteev, E. V. Chulkov, F. J. García de Abajo, and J. E. Ortega, Phys. Rev. B **66**, 245419 (2002).

[3] V. A. Shchukin and D. Bimberg, Rev. Mod. Phys. **71**, 1125 (1999).

[4] R. Notzel, Z. C. Niu, M. Ramsteiner, H. P. Schonherr, A. Tranpert, L. Daweritz, and K. H. Ploog, Nature (London) **392**, 56 (1998).

[5] D. Qin, Y. N. Xia, B. Xu, H. Yang, C. Zhu, and G. M. Whitesides, Adv. Mater. (Weinheim, Ger.) **11**, 1433 (1999).

[6] A. A. Golovin, M. S. Levine, T. V. Savina, and S. H. Davis, Phys. Rev. B **70**, 235342 (2004).

[7] R. J. Asaro and W. A. Tiller, Metall. Trans. **3**, 1789 (1972).

[8] M. A. Grinfel'd, Sov. Phys. Dokl. **31**, 831 (1986).

[9] P. W. Tasker, J. Phys. C **12**, 4977 (1979).

[10] K. Radican, N. Berdunov, G. Manai, and I. V. Shvets, Phys. Rev. B **75**, 155434 (2007).

[11] J. Gustafson *et al.*, Phys. Rev. Lett. **92**, 126102 (2004).

[12] C. T. Campbell, Phys. Rev. Lett. **96**, 066106 (2006).

[13] M. Todorova, W. X. Li, M. V. Ganduglia-Pirovano, C. Stampfl, K. Reuter, and M. Scheffler, Phys. Rev. Lett. **89**, 096103 (2002).

[14] M. W. Finnis, J. Phys.: Condens. Matter **8**, 5811 (1996).

[15] R. Benedek, A. Alavi, D. N. Seidman, L. H. Yang, D. A. Muller, and C. Woodward, Phys. Rev. Lett. **84**, 3362 (2000).

[16] I. Horcas, R. Fernández, J. M. Gómez-Rodríguez, J. Colchero, J. Gómez-Herrero, and A. M. Baro, Rev. Sci. Instrum. **78**, 013705 (2007).

[17] B. Brandt and A. Stapski, Acta Chim. Slovenica **21**, 661 (1967).

[18] V. Bhosle, A. Tiwari, and J. Narayan, J. Appl. Phys. **97**, 083539 (2005).

[19] M. Henzler, Appl. Phys. **9**, 11 (1976).

[20] M. Horn–von Hoegen, Z. Kristallogr. **214**, 684 (1999).

[21] P. M. Oliver, G. W. Watson, E. T. Kelsey, and S. C. Parker, J. Mater. Chem. **7**, 563 (1997).

[22] A. Howard, C. Mitchell, D. Morris, R. Egdell, and S. Parker, Surf. Sci. **448**, 131 (2000).

[23] F. Jones, R. Egdell, A. Brown, and F. Wondre, Surf. Sci. **374**, 80 (1997).

[24] G. Kresse and J. Furthmuller, Phys. Rev. B **54**, 11169 (1996).

[25] P. E. Blöchl, Phys. Rev. B **50**, 17953 (1994).

[26] G. Kresse and D. Joubert, Phys. Rev. B **59**, 1758 (1999).

[27] D. M. Ceperley and B. J. Alder, Phys. Rev. Lett. **45**, 566 (1980).

[28] A. F. Andreev, Zh. Eksp. Teor. Fiz. **80**, 2042 (1981).

[29] V. I. Marchenko, Zh. Eksp. Teor. Fiz. **81**, 1141 (1981).

[30] S. Rousset, V. Repain, G. Baudot, Y. Garreau, and J. Lecoeur, J. Phys.: Condens. Matter **15**, S3363 (2003).

[31] J. J. Metois, A. Saul, and P. Muller, Nat. Mater. **4**, 238 (2005).

[32] M. Huth, K. Ritley, J. Oster, H. Dosch, and H. Adrian, Adv. Funct. Mater. **12**, 333 (2002).

[33] M. D. Segall, P. J. D. Lindan, M. J. Probert, C. J. Pickard, P. J. Hasnip, S. J. Clark, and M. C. Payne, J. Phys.: Condens. Matter **14**, 2717 (2002).

[34] D. Vanderbilt, Phys. Rev. B **41**, 7892 (1990).

[35] B. B. Karki, L. Stixrude, S. J. Clark, M. C. Warren, G. J. Ackland, and J. Crain, Am. Mineral. **82**, 51 (1997).

[36] S. Shang, Y. Wang, and Z.-K. Liu, Appl. Phys. Lett. **90**, 101909 (2007).

[37] R. Shuttleworth, Proc. Phys. Soc., London, Sect. A **63**, 444 (1950).